Influence of wetting–drying cycles on the compression behavior of a compacted loess from microstructure analysis

Kangze Yuan[1,2] · Wankui Ni[1] · Xiangfei Lü[1,3,4] · Gabriele Della Vecchia[2] · Haiman Wang[1] · Lan Li[1] · Yongpeng Nie[1]

Abstract

This study explores the compression deformation characteristics of compacted loess after different wetting–drying (WD) cycles, by tracking microstructure changes by scanning electron microscope (SEM), laser particle size analyzer, Fourier transform infrared spectroscopy (FTIR), and nuclear magnetic resonance (NMR). Experimental results show that, as the number of wetting–drying cycles increases, the compression deformation of the compacted loess upon mechanical loading increases and the yield stress decreases. The first wetting–drying cycle causes the largest change in terms of mechanical response. As long as the number of wetting–drying cycles increases, their effect is less significant. Microstructural analyses have been exploited to interpret the evolution of the mechanical properties at the laboratory scale. With the increase in the number of wetting–drying cycles, FTIR results showed that the functional group strength gradually decreased, implying a reduction of the cementation strength between the particles of the compacted material. SEM images showed that the contacts among loess aggregates (composed by particles) varied from "face to face" to "point to point." NMR results demonstrated that the total and inter-aggregate pores volume increased, while the intra-aggregate pores volume decreased upon wetting–drying cycling. The microstructure investigation allowed understanding the major role played by cementation strength, aggregate contact type, and pore size distribution on the compression behavior of compacted loess after wetting–drying cycles.

Introduction

Loess is a special sediment formed under arid and semi-arid climate conditions during the Quaternary Period (Shi and Shao 2000; Rost 2001; Nicolli et al. 2010; Yu et al. 2019). Its particular microstructural arrangement is characterized by high porosity and by a silt-dominated particle size, with an open fabric supported by cementation bonds. These features cause the peculiar engineering properties of loess (Lv et al. 2014; Wang et al. 2019a, b). Among them, loess sediments may experience sudden volumetric collapse upon both mechanical loading and wetting processes, causing relevant damages to infrastructure founded on these formations (Wang et al. 2011; Yao et al. 2020a, b; Zhang et al. 2020). As a consequence, it is often necessary to improve loess mechanical properties through artificial techniques, to make them suitable to fulfill the requirements of engineering construction. Compaction methods, such as static compaction, dynamic compaction, and chemical stabilization, are considered able to provide sufficient strength and stiffness to the loess material to meet construction requirements (Mariri et al. 2019; Meng and Li 2019). Although the compacted loess can meet the engineering requirements from the mechanical point of view (i.e., sufficient strength and stiffness as a foundation material), wetting–drying cycles (WD cycles) caused by subsequent rainfall and evaporation processes have proven to decrease loess strength and induce relevant deformation (Yao et al. 2020a, b). Collapse and serviceability issues for infrastructures built on compacted

✉ Wankui Ni
niwankui@chd.edu.cn

1 College of Geological Engineering and Geomatics, Chang'an University, No. 126 Yanta Road, Shaanxi 710054 Xi'an, People's Republic of China

2 Department of Civil and Environmental Engineering, Politecnico di Milano, Piazza Leonardo da Vinci, 32, 20133 Milan, Italy

3 School of Water and Environment, Chang'An University, No. 126 Yanta Road, Xi'an, Shaanxi 710054, People's Republic of China

4 CCCC First Highway Consultants Co., LTD, No. 205 Science and Technology Road, Xi'an, Shaanxi 710075, People's Republic of China

loess foundations due to absolute and/or differential settlements after WD cycles have been recently evidenced by Zhang et al. (2019), Li et al. (2018), and Qi et al. (2008). Several researches have been carried out in order to understand the effect of WD cycles on the mechanical behavior of compacted loess. A decrease in unconfined compressive strength, cohesion, and elastic stiffness of loess specimens for an increasing number of WD cycles has been identified by Pinyol et al. (2007), together with an increase in one-dimensional compressibility and collapse deformation. Arthur et al. (2013) performed uniaxial confined compression tests and found that the WD cycles reduced the preconsolidation stress and compressibility of the loess samples. WD cycles have been also proved not only to reduce the bonding strength between particles, but also to increase void ratio and permeability, vanishing the effects of chemical stabilization (Lu et al. 2015). Consistent evidences have been also provided by Mao et al. (2013), which showed void ratio increase and cohesion decrease with WD cycles, and Zhang et al. (2017), which reported the influence of WD cycles on the dissolution of cement bondings, expansion of cracks and fissures, change in pore structure, and reduction in water retention capacity.

The microstructure of loess plays a very important role on its compression behavior (Hu and Cheng 2017; Ma et al. 2020; Ni et al. 2020). Wang et al. (2020a, b) reported that the mesopore content (10~35 μm) of compacted loess increased significantly with the increase of the number of wetting–drying cycles. The role of particle size on particle disintegration has been studied by Ono et al. (2020), who performed triaxial compression tests on sedimentary rock specimens after the WD cycle. Rosone et al. (2018) conducted MIP tests on lime-treated clay before and after WD cycles, proving that the pore size distribution of the material changed, passing from an initial bimodal pore size distribution to a unimodal one. Experimental evidence on the impact of drying–wetting cycles on the water retention, hydraulic conductivity, and fabric of compacted silt specimens have also been recently presented by Azizi et al. (2020) and Musso et al. (2020), who evidenced fabric changes without significant volumetric strains, which induced an increase of hydraulic conductivity and a reduction in the retention capacity compared to the as-compacted material.

Despite the evolution of mechanical properties and microstructure of compacted loess under different WD cycles have been documented by several authors, no quantitative microstructural evaluation of compacted loess cementation strength has been provided yet. Current knowledge on this aspect has been just exploited to link compacted loess cementation strength to mechanical properties at the laboratory scale. As for pore size distribution changes, this aspect has been mainly investigated in the literature through MIP testing (Sun et al. 2020; Wang et al. 2020a, b). Beyond the well-known problem due to the fact that MIP underestimates the amount of micropores (due to the limited injection capacity of the experimental device), a peculiar limitation of MIP for loess stems from its fragile and complex internal microstructure. MIP measurement in fact has been proven to induce significant damage to loess structure (Tian et al. 2014), changing the structure of internal pores and thus leading to inaccurate experimental results.

Based on the above considerations, this study first presents experimental results about the compression behavior of compacted loess specimens after different number of WD cycles, and then provides a microstructural interpretation considering different aspects of loess microstructure, including (i) cementation strength, (ii) aggregate contacts, (iii) particle size distribution, and (iv) pore size distribution (Shao et al. 2018). Cementation strength evaluation relies on FT-IR spectra, to calculate the strength of functional groups on the loess surface. The size of the particles is estimated by a laser particle size analyzer, and particle contact relation is observed on the surface of the loess by SEM photomicrographs. The pore size distribution is finally evaluated via NMR, a non-destructive testing method that ensures that the original microstructure of the compacted loess after different WD cycles is preserved. The innovative contribution of this study relies on the capacity of providing a sound microstructural interpretation for the compression behavior of compacted loess due to increasing number of WD cycles.

Materials and methods

The study location

The Luochuan Loess National Geopark is located in Luochuan County, south of Yan'an City, Shaanxi Province (Fig. 1). It is famous not only for its typical loess-paleosol sequences (i.e., stratigraphy relic), but also for some unique loess landscapes (i.e., geological landform) (Wang et al. 2019a, b). The area is characterized by a semi-arid continental monsoon climate. The average annual temperature is 7.7–10.6 °C. The extreme values of the average temperature by month are −28.5 °C in January and 39.9 °C in July (Chen and Wang 2014). The average annual precipitation is 490.5–663.3 mm. The distribution of precipitation throughout the year is uneven, with the maximum precipitation occurring in summer and the minimum in winter (Zhu et al. 2020).

Original loess material

The investigated samples were retrieved from a foundation pit at a depth of 6.5–7 m below the ground surface. The retrieved material can be classified as Malan loess (Liu 2016). In order to minimize sampling disturbance, all
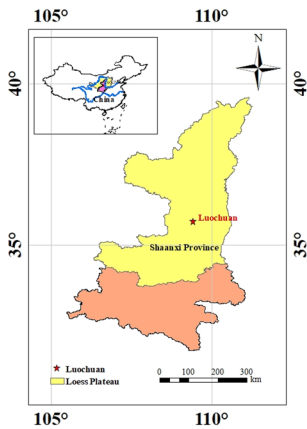
Fig. 1 Major occurrence of the Loess Plateau in China and sampling location at the excavation site (latitude 35°42′46.09″, longitude 109°26′0.10″)

the samples were retrieved by hand, sealed with a plastic film inside a cylindrical iron bucket, and transported to the laboratory. The physical properties of the retrieved material were determined following ASTM (2006) test methods. According to the XRD pattern of the original loess (Fig. 2), the quantitative mineralogical composition was calculated. Physical parameters, Atterberg limits, and the mineralogical composition of the loess samples are listed in Table 1.

Preparation of the specimens

After the original loess collection, the experimental specimens were prepared as follows. Firstly, the original loess was crushed with a wooden hammer until all aggregates are destroyed. The crushed material was then passed
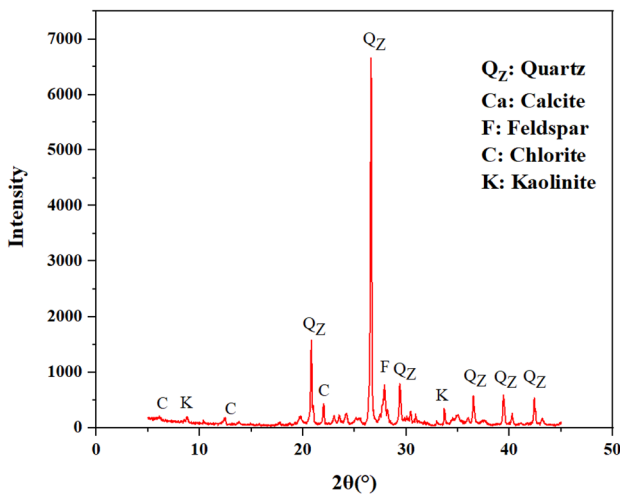

Fig. 2 XRD pattern of the original loess sample

Table 1 Properties of the loess used in this study

Quantity	Value
In situ density (g/cm^3)	1.33 ~ 1.40
Natural water content (%)	12
Specific gravity of solids	2.71
Plastic limit (ω_P/%)	19.5
Liquid limit (ω_L/%)	28.8
Plasticity index (I$_p$ /%)	9.3
Quartz (%)	51.1%
Feldspar (%)	7.70%
Calcite (%)	15.2%
Chlorite (%)	9.00%
Kaolinite (%)	2.90%

through a 2 mm sieve, oven-dried at 105 °C for 8 h (up to $w_0 = 0\%$) and finally cooled at room temperature. Thereafter, an amount of deionized water, calculated from Eq. (1), was gradually added to the material using a spray bottle, until it reached the target compaction water content ($w = 12\%$). The target compaction water content has been set equal to the natural water content, in order to reduce the influence of the initial water content on the experimental findings (Hong et al. 2010):

$$m_w = \frac{0.01 \times (w - w_0)}{1 + 0.01 w_0} \times m_0 \tag{1}$$

where m_w is the mass of deionized water added, m_0 is the mass of the soil sample after drying, w is the target compaction water content, and w_0 is the initial water content, i.e., the water content of the material after oven-drying ($w_0 = 0\%$). Crushed hydrated loess was then tightly sealed with plastic film and placed in a humidor for about 48 h at room temperature. Part of the processed loess was used for water content check. If the difference between the average water content after retesting and the target water content was within ± 0.2%, the sample preparation process could begin. Finally, the material was compacted directly in an oedometer cell. After compaction, the specimens was characterized by a height of 20 mm, a diameter of 79.8 mm, a dry density of 1.35 g/cm^3, and a water content of 12%.

Wetting–drying cycle testing

Each wetting–drying (WD) cycle was carried out on the loess specimens prepared in the oedometer cell (as described in "Preparation of the specimens" section) according to the following procedure: (1) the specimens were firstly saturated for 12 h in the mold under vacuum conditions. They are considered saturated according to GB/T 50,123–1999 (National standards of People's

Republic of China 1999); (2) the saturated specimens were completely oven dried by exposure to air at 105 °C for 8 h, reaching a complete dry state ($w = 0\%$) based on the results of ASTM. D2974-07a (2007); (3) the dried specimens were finally brought to the water content of 12% according to the same procedure shown in "Preparation of the specimens" section; (4) finally, the loess specimens were then sealed in polythene wraps for a period of at least 24 h to achieve a uniform water distribution after each WD cycle. Upon wetting–drying cycles, the material ranges between a saturated and a dry state. During the wetting–drying cycles, the height of the samples was also measured, using a Vernier caliper with a resolution of 0.01 mm. Specimen height was found to change slightly, as in Mu et al. (2020). Different numbers of WD cycles were performed, namely 1, 3, 5, 10, 15, and 20. For each WD cycle, at least two samples were collected: one for oedometer testing, the other one for microstructural characterization. For comparison, the loess samples that have not undergone any WD cycles are indicated as 0 WD cycles.

Oedometer tests

After being subjected to WD cycles, specimens were subjected to oedometer testing. Specimens were cut into a standard 79.8 mm (diameter) × 20 mm (height) cutting ring (with the specimen confined in the ring to prevent radial deformation), and placed between two porous stones. The piston of the cell, which was fixed to the upper porous stone, was in contact with the loading ram, whose displacement is accurately measured with a dial gauge. All specimens were subjected to increasing vertical stresses of 50 kPa, 100 kPa, 150 kPa, 200 kPa, 300 kPa, 400 kPa, 600 kPa, and 800 kPa. The confined compression strain ε_{si} has been obtained as:

$$\varepsilon_{si} = \frac{h_0 - h_i}{h_0} \times 100\% \tag{2}$$

where h_0 is the initial specimen height, and h_i is specimen height at the end of each loading step, after excess pore pressure dissipation.

Microstructural characterization

Samples subjected to the WD cycles were also carefully selected for microstructural characterization. Then, 1 cm × 1 cm × 2 cm (length × width × height) cuboids were trimmed out from the central part of the loess samples. In order to minimize the impact of preparation work, appropriate sample drying methods should be used (Russ 1992). Despite freeze-drying can be preferred to other preparation techniques

because of the very limited effect on the original structure of the sample (Ahmed et al. 1974; Delage and Pellerin 1984; Romero and Simms 2008), air-drying has been also widely used in soil science (Bai 1992), mostly because of its economy and simplicity. Samples were air-dried in the laboratory environment (temperature of 20 ± 2 °C and 50% of relative humidity), allowing the soil to slowly lose water (e.g., Dathe et al. 2001). This process took around 30 days. Careful measurements were performed to check the change in volume of the samples due to air-drying, which was found to remain lower than 1%. Due to the negligible shrinkage induced by air-drying, the effect on loess material micro-structure has been considered negligible, as in Ma et al. (2017). After drying, half of the cuboid is stuck to the shooting pad for sputter coating with platinum (Pt) in a sputtering ion equipment, using an electron-conductive tape without disturbing the fractured plane. A FEI MLA650F SEM was used to record the microstructure images of all samples. FT-IR spectra measurement surface group of loess samples were registered in KBr using a Thermoelectric Nicolet iS51. The particle size distribution of loess samples was determined by Bettersize 2000 Intelligent Laser Particle Size Analyzer in a range of 0.02 μm to 2000 μm.

Geophysical NMR methods were used to analyze the distributions of pore size in loess samples by MacroMR12-150H-1. According to the literature (Costabel and Yaramanci 2013; Houston et al. 2001), it is well known that (i) the amplitude of the ^1H protons NMR signal in water molecules of the loess sample is proportional to the water content and (ii) the relaxation times (T_2) provides information on pore size distributions when the sample is placed in a magnetic field and excited with a brief pulse of radio frequency (RF) energy. The relaxation time (T_2) is the transverse relaxation time of the pore water among the loess particles, as measured by a Carr-Purcell-Meiboom-Gill (CPMG) sequence. It is a measure of the rate at which the precession of hydrogen nuclei in the formation pore water gradually decay in the presence of an inhomogeneous magnetic field, which can be used to calculate the pore size distributions of loess samples, as described in the following. From the description above, it can be inferred that the presence of pore water in loess voids is a necessary condition for this measurement. Thus, the compacted loess samples from the cutting ring were saturated under vacuum conditions and fixed in a specially-made quartz tube (diameter 23 mm × height 20 mm). The quartz tube containing the sample was finally placed in the testing tube to obtain the T_2 curve. A schematic of this process is shown in Fig. 3.

For water-saturated loess samples, T_2 can be obtained from Eq. (3), based on the NMR relaxation mechanisms (Kong et al. 2018):

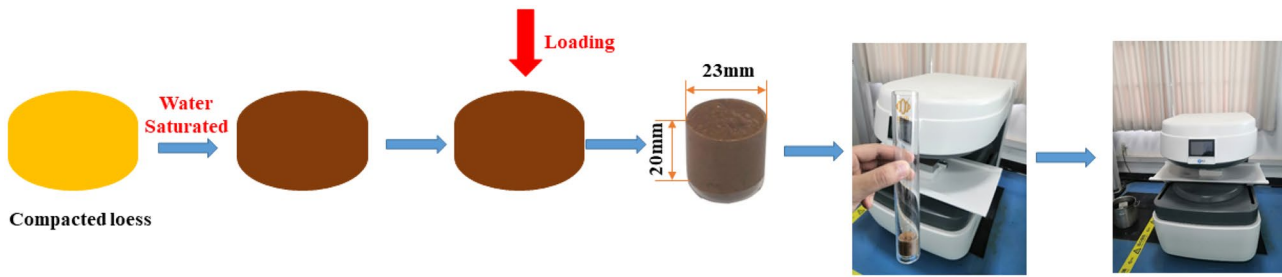$$\frac{1}{T_2} = \frac{1}{T_{2B}} + \frac{1}{T_{2S}} + \frac{1}{T_{2D}} \tag{3}$$

Fig. 3 NMR sample preparation and test process

T_{2B} is the bulk water relaxation time, T_{2S} is the surface-enhanced relaxation time at the pore walls, and T_{2D} is the diffusion relaxation time, which accounts for the transverse relaxation in an inhomogeneous magnetic field. For water, T_{2B} is much larger than T_{2S} and T_{2D}, so the contribution of T_{2B} on T_2 can be neglected. For loess pore water, T_2 is then is directly related to the internal pore structure of the loess, as

$$\frac{1}{T_2} = \frac{1}{T_{2S}} = \rho \frac{S}{V} = \rho \frac{\alpha}{r} \tag{4}$$

where ρ (expressed in general in μm/s) is the surface relaxivity coefficient, characterizing the magnetic interactions at the water-loess particles interface, and S/V is the ratio between the pore surface area S to the pore water volume V. The ratio S/V is proportional to the reciprocal of pore radius r, expressed as $\frac{\alpha}{r}$. The geometry factor α in Eq. (4) depends on the pore shape, e.g., $\alpha = 1$ for planar pores, $\alpha = 2$ for cylindrical pores (as assumed in this study), and $\alpha = 3$ for spherical pores. Hence, Eq. (4) finally reads:

$$\frac{1}{T_2} = \rho \frac{\alpha}{r} = \rho \frac{2}{r} \tag{5}$$

or

$$T_2 = \frac{1}{2\rho} r \tag{6}$$

To determine the surface relaxivity coefficient ρ, a widely accepted NMR-permeability equation, known as Schlumberger-Doll Research (SDR) equation developed by Kleinberg (1996), is used. The SDR equation links the surface relaxivity coefficient (ρ) to soil saturated permeability k_s as

$$k_s = C \varnothing^4 T_{2LM}^2 \tag{7}$$

being the constant C expected to coincide with the square of the surface relaxivity coefficient (Kleinberg et al. 2003), $\varnothing$ is porosity and T_{2LM} is the geometric mean value of the T_2 distribution.

This dependence of the saturated permeability of the soil k_s (measured on the virgin compression curve, generally expressed in m²) on ρ may be expressed as

$$k_s = \rho^2 \varnothing^4 T_{2LM}^2 \tag{8}$$

leading to

$$\rho = \sqrt{\frac{k_s}{\varnothing^4 T_{2LM}^2}} \tag{9}$$

In this study, values of $k_s = 3.66 \times 10^{-14}$ m², $\varnothing = 0.50$, and $T_{2LM} = 0.5324$ ms have been considered. The resulting ρ value was 1.4375 μm/ms.

Results and discussion

FTIR of loess samples after different WD cycles

FT-IR spectroscopy is a useful technique to investigate the functional groups adsorbed onto the surface of loess particles. In order to compare the effect of different WD cycles on the surface group of loess particles, loess samples have been subjected to the same WD cycle number considered in the previous section, and then used to collect spectra, allowing a quantitative comparison between loess particles. Experimental results are illustrated in Fig. 4. The x-axis represents the wavenumber, which is related to the functional groups. The y-axis represents the transmittance: the lower the transmittance, the higher the strength of the functional group. The results indicated that the seven spectra of the loess were very similar. The seven FTIR spectra indicated the presence of five strong absorption bands at 3624 cm⁻¹, 1437 cm⁻¹, 1032 cm⁻¹, 825 cm⁻¹, and 472 cm⁻¹, respectively. The absorption peak in 3624 cm⁻¹ was associated with the stretching vibrations of surface hydroxyl groups of loess particles, whereas the band around 1437 cm⁻¹ was attributed to the bending vibration of carbonate groups CO_3^{2-} (Huang et al. 2018). The strong

**Fig. 4** FTIR spectra of loess samples subjected to different WD cycles
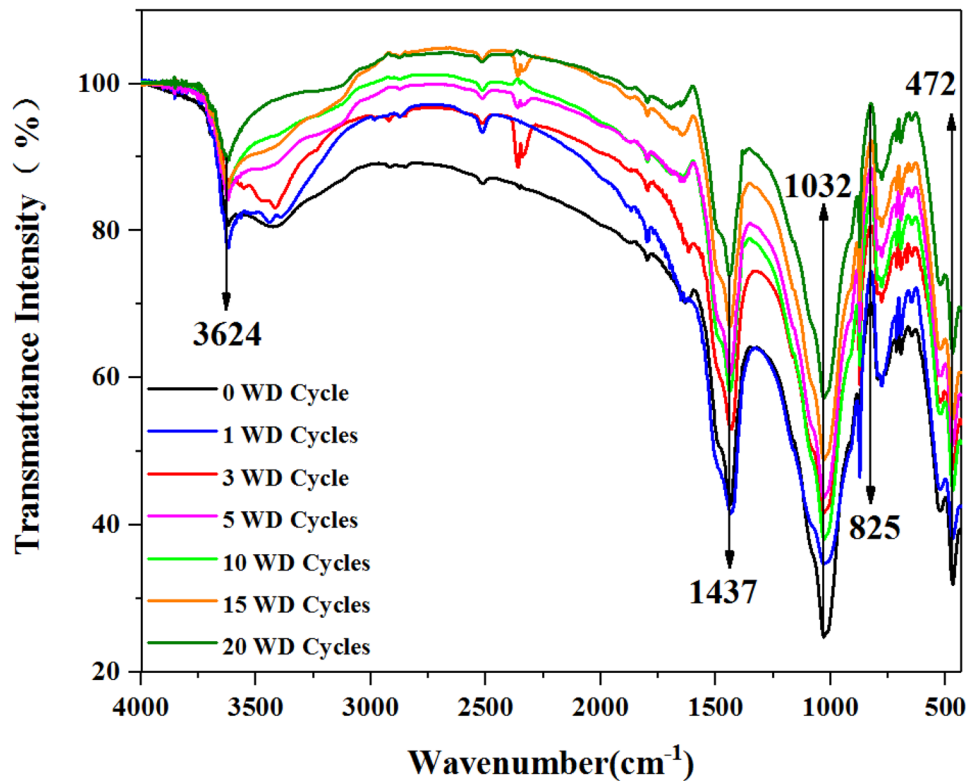
and broad peaks around 1032 cm⁻¹ were attributed to the antisymmetric stretching vibration peak of Si–O–Si, while the sharp peaks observed at both 825 cm⁻¹ and 472 cm⁻¹ could be ascribed to the symmetric stretching vibration peak of Si–O–Si, indicating the presence of SiO_4^{2-} on the surface of all samples. These observations confirm that hydroxyl groups, carbonates, and silicate anions were present on the surface of loess particles.

It is evident that the surface of loess samples after different WD cycles exhibited fewer numbers of hydroxyl groups than that of loess before WD cycling. It was hypothesized that hydroxylation levels play a role in the interaction between adjacent loess particles. According to the intensity changes of hydroxyl groups, it can be inferred that the salts on the surface of loess particles were removed away during WD cycles, resulting in the decreasing number of hydroxyl groups. From the FT-IR spectra intensity of the seven loess samples after different WD cycles, it follows that the interaction between adjacent loess particles after WD cycles became weaker as long as the number of WD cycle increases. Vice versa, the loess particles not subjected to WD cycles are characterized by a larger number of OH⁻ group, which could provide more hydrogen group for the interaction between the adjacent loess particles, as proved in the following.

Morphology of loess after WD cycles

Figure 5 shows a schematic of the three typical possible contacts between adjacent loess aggregates. Aggregates are usually formed by the association of individual sand, silt, and clay particles (Vasava et al. 2019), and their contacts control the onset of relative movement between aggregates. Fang and Shen (2013) proposed two main contact relationships between aggregates, based on the contact area and the amount of clay, namely "direct" and "indirect" contact. Direct contacts between aggregates are mostly sensitive to mechanical forces, while indirect contacts (usually characterized by thin layer of clay at the point of contact, as described by Li et al. 2016) are more sensitive to the presence of water. Water can soften the cementing material and weaken aggregate cementation, up to the disruption of the connection between aggregates and to local collapse upon wetting. In this study, the influence of edge to edge contacts on loess structure has also been evidenced: their contact area is intermediate between the point to point and the face to face ones. Also edge to edge contacts may be both direct and indirect. Note that the structural strength of compacted loess increases as the contact area between aggregates increases (Li et al. 2019). Thus, the largest structural strength is obtained for face to face contacts, while the lowest strength is related to point to point contacts. The morphology of the compacted

Fig. 5 Schematic illustration of aggregate contacts
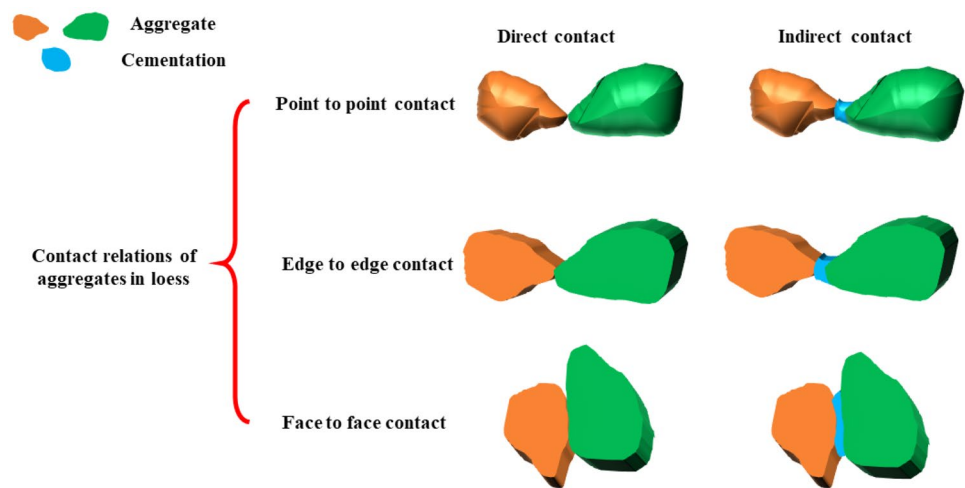
loess is compared at 800 times magnification for different WD cycles (Fig. 6). Figure 6A~G show the images of loess samples after 0, 1, 3, 5, 10, 15, 20 WD cycles, respectively. In Fig. 6A, corresponding to 0 WD cycles, the connections between the aggregates are densely arranged, and there are a few inter-aggregate pores. Contacts between aggregates are mainly face to face. After 1 WD cycle, the number of inter-aggregate pores increase, but the connection between the aggregates is still predominantly face to face (Fig. 6B). Increasing the number of WD cycles, the connection between the aggregates is gradually loosened and more inter-aggregate pores appear (Fig. 6C). For the samples after 5 WD cycles, the number of edge to edge contacts between aggregates appears to increase, and the number of face to face contacts appears to decrease, compared to the samples subjected to a lowest number of cycles (Fig. 6D). After 10 WD cycles, the number of point to point contacts significantly increases, and the presence of large inter-aggregate pores is evident (Fig. 6E). After 15 (Fig. 6F) and 20 (Fig. 6G) WD cycles, the changes in surface morphology are slight, compared with Fig. 6E. As for the type of contact between loess particles, the number of face to face contacts then gradually decreases upon WD cycling, while the number of edge to edge contacts and point to point contacts gradually increases.

Particle size distribution of loess samples after WD cycles

A laser particle sizer was used to evaluate the changes in loess particle size distribution after WD cycles. In order to validate the laser diffraction measurement of particle size distribution, the classical sieving and picnometer methods have been also used, to measure the granulometric distribution of the 0 WD sample. The particle size distribution was determined by sieving through aperture sizes of 2 mm, 1 mm, 0.5 mm, 0.25 mm, and 0.075 mm. Particles with a diameter smaller than 0.075 mm were analyzed with a picnometer using the SediGraph method. A dispersing agent (sodium hexametaphosfate) was added to the soil–water mixture before the sedimentation test, in order to avoid particle flocculation. The cumulative particle volume curves of the 0 WD samples, obtained via both the classical method and laser diffraction, are shown in Fig. 7A: very small differences were obtained. Figure 7B shows the frequency distribution curves of loess samples, obtained by laser diffraction measurements, after different WD cycles. All the particle size distributions presented a bimodal curve, typical of loess (Sun et al. 2004; Vandenberghe 2013). The particle sizes span the range 0.06–188.5 μm and the frequency curves are asymmetric. Particle sizes can be classified based on the content of clay (particle size < 2 μm), silt (2–50 μm), and sand (50–2000 μm) particles, e.g., according to U.S. Department of Agriculture (USDA). Table 2 presents the volume proportion of the different particle categories in the compacted loess samples after different WD cycles. It can be seen that the composition of the compacted loess is still dominated by silt independently from the number of WD cycles, and that the proportion of each class of particles is hardly affected. Similar results were also obtained by Shao et al. (2018).

Pore size distribution of loess samples after WD cycles

As discussed in "Oedometer tests" section, NMR signal intensity is proportional to the water content, which is related to pore abundance. The distribution curves of relaxation time T_2 of loess samples are shown in Fig. 8, showing bimodal relaxation distributions: short relaxation times correspond to small pores, while long relaxation times correspond to large pores. According to the SEM images, where aggregates and inter-aggregate pores were identified, the bimodal relaxation distribution curves confirm that both intra-aggregate pores (micropores) and inter-aggregate pores (macro-pores) are present in
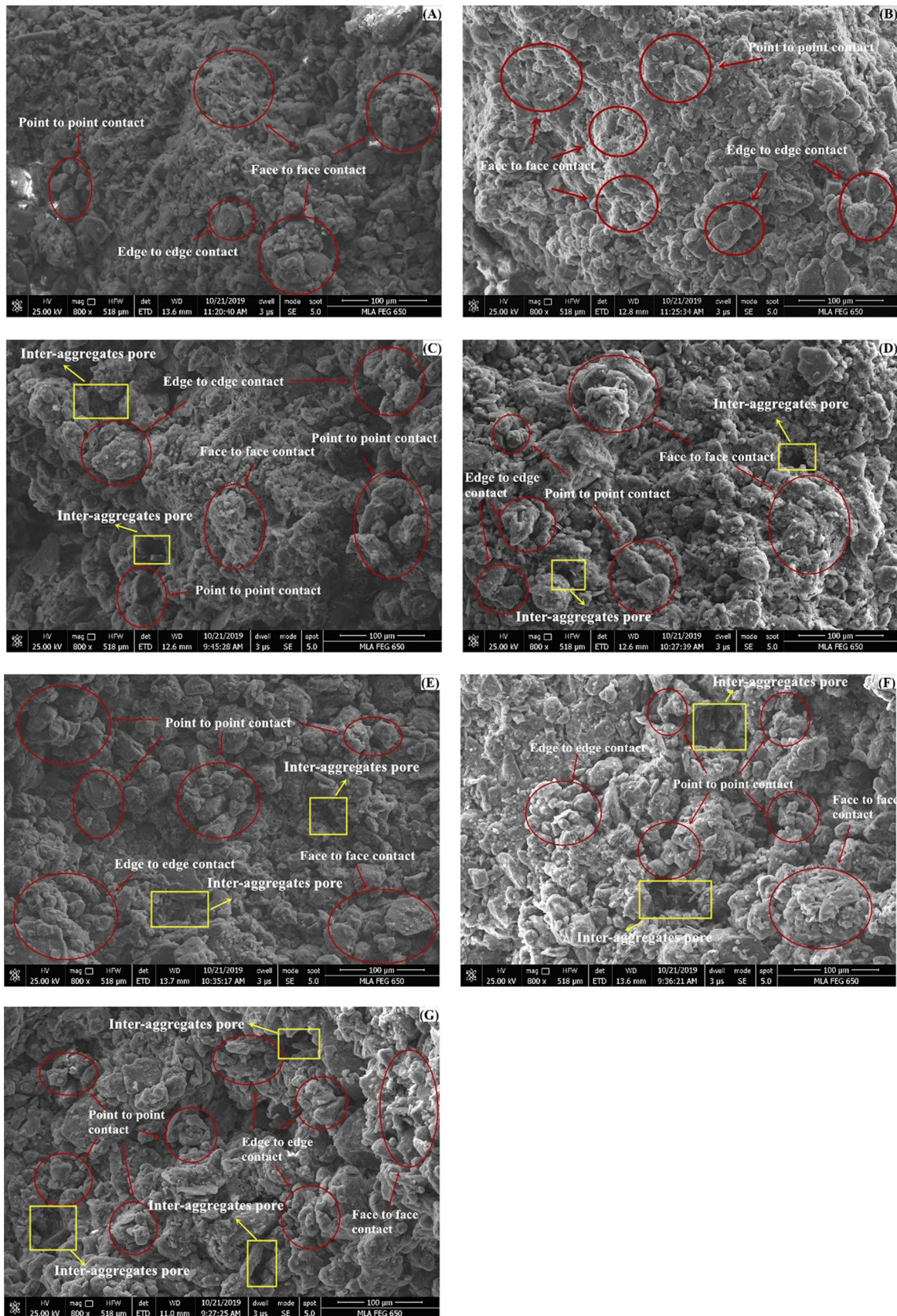
Fig. 6 SEM images of loess after different WD cycles (**A**: no cycles; **B**: 1 cycle; **C**: 3 cycles; **D**: 5 cycles; **E**: 10 cycles; **F**: 15 cycles; **G**: 20 cycles)
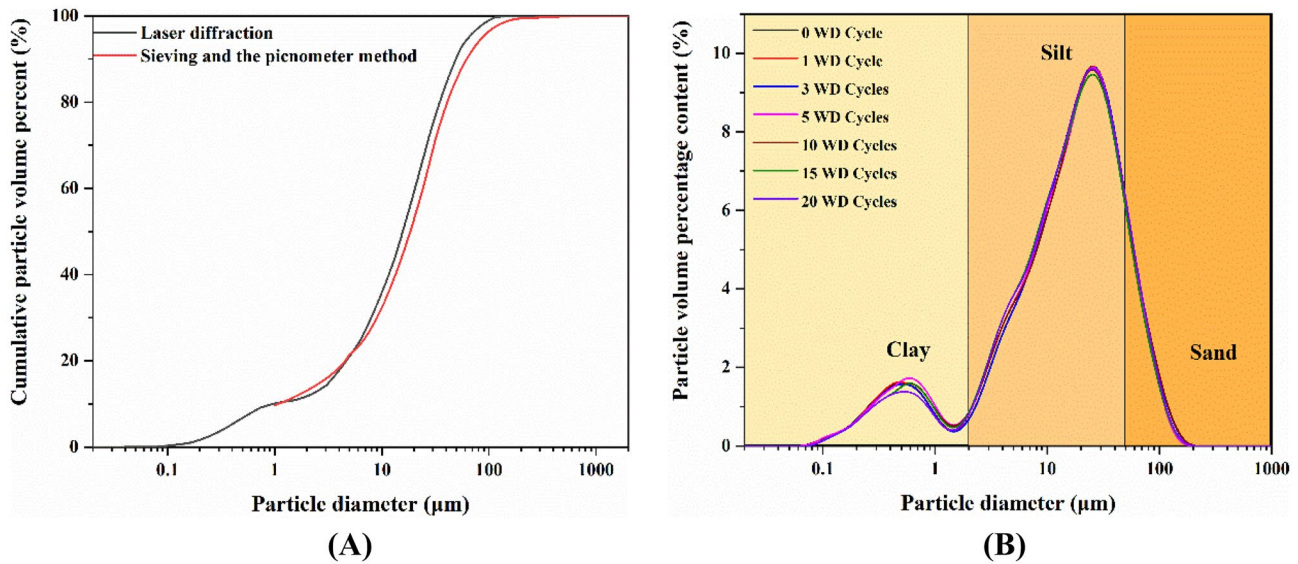
Fig. 7 **A** Cumulative particle volume curve of the 0 WD samples and **B** particle size distributions of loess samples after WD cycles

Table 2 Volume proportion of clay, silt, and sand particles after different WD cycles

		Number of WD cycle						
		0	1	3	5	10	15	20
Particle volume percentage (%)	Clay	11.32	11.32	12.32	12.32	11.63	11.61	10.16
	Silt	76.30	76.30	76.27	76.27	75.81	77.12	77.68
	Sand	12.38	12.38	11.41	11.41	12.56	11.27	12.16

all loess samples. According to Eq. (6) and Fig. 8, the pore size distribution curve and cumulative NMR intensity curve of compacted loess after different WD cycles can be obtained (as shown in Fig. 9). The results show that the bimodal pore
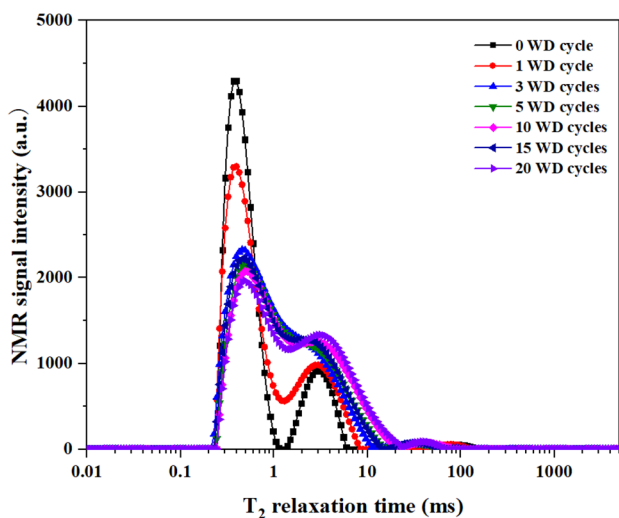

Fig. 8 Variation of T_2 distribution curves under different WD cycles

distribution of all samples mainly consists of a pore diameter ranging from 1.202 to 879.521 μm. The as-compacted PSD function has been used to identify a discriminating pore size between intra-aggregate and inter-aggregate porosity (see, e.g., Romero et al. 2011; Della Vecchia et al. 2015): data shown in Fig. 9a suggests a discriminating pore size between intra- and inter-aggregate voids of 6.9 μm. For any sample subjected to WD cycles, the pore volume corresponding to a pore size lower than 6.9 μm is attributed to intra-aggregate pores, while the pore volume corresponding to a pore size larger than 6.9 μm is attributed to inter-aggregate pores. Figure 10 shows the changes in cumulative NMR intensity corresponding to intra-aggregate pore volume, inter-aggregate pore volume, and total pore volume after different WD cycles. For intra-aggregate pores, the decrease of cumulative NMR intensity from the initial value is 13.59%, 30.58%, 35.81%, 39.40%, 39.42%, and 42.46%, for 1, 3, 5, 10, 15, and 20 cycles, respectively; while an increase of about 71.16%, 161.27%, 192.36%, 224.05%, 225.51%, and 238.55% is obtained for the NMR intensity corresponding to inter-aggregate pores. As for total pore volume, the relative increase of pore volume is 4.12%, 9.50%, 11.85%, 15.63%, 15.92%, and 16.24%, for 1, 3, 5, 10, 15, and 20 cycles respectively. WD cycling thus seems to
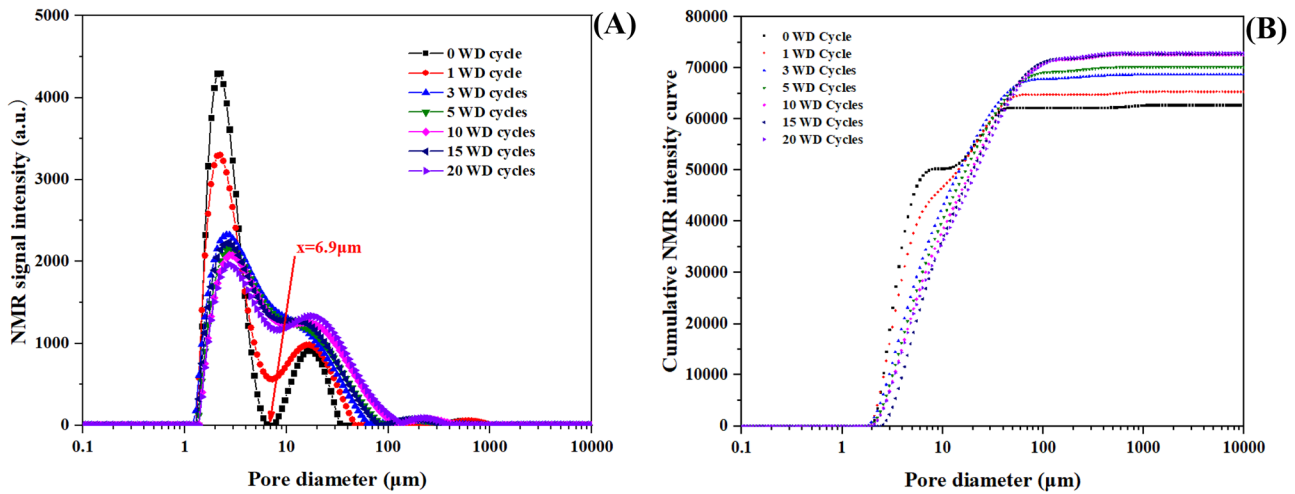
Fig. 9 A Pore size distribution curve in terms of NMR intensity and **B** cumulative NMR intensity curve after different WD cycles

induce a reduction in intra-aggregate porosity and as a consequence an increase in inter-aggregate porosity, that cannot be explained by the total volume increase alone. As expected, the larger effect on pore size distribution is obtained after the first WD cycle; as long as the number of cycles is increased, the effects are less significant. After 10 cycles, further WD cycles seem not to affect material fabric anymore, consistently to "Morphology of loess after WD cycles" section.

Compression behavior of loess after WD cycles

After being subjected to WD cycles, specimens were loaded in oedometer in order to evidence the role of WD cycles on material compressibility. After different WD cycles, the measured compression strain of loess samples for each vertical loading is shown in Fig. 11. The application of a vertical stress of 800 kPa causes confined compression strain with values ranging from 1.25 to 17%. As expected, from the mechanical point of view a locking response is obtained, with one-dimensional stiffness increasing with the applied vertical loading. Interestingly, the compression behavior of compacted loess samples is closely related to the number of WD cycles experienced before loading. The larger the number of WD cycles applied, the larger the confined compression strain at the end of the loading stage: the largest confined compression strain (17%) was in fact recorded for the maximum number of WD cycles (20). The effect on the following mechanical response of each WD cycle reduces
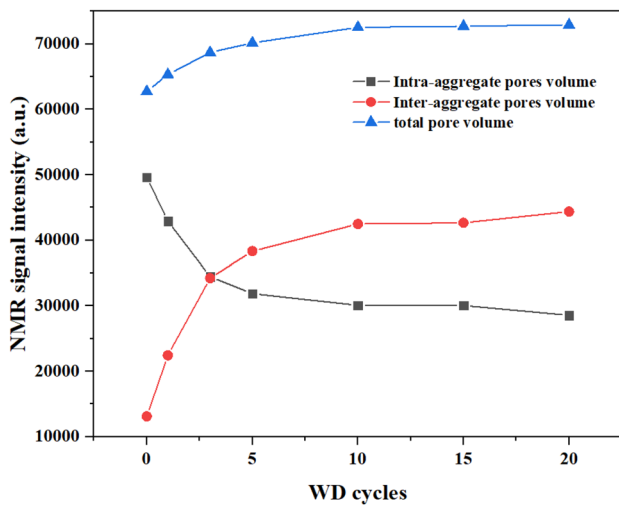

Fig. 10 Variations in volume of intra-aggregate, inter-aggregate and total pore volume, expressed in term of NMR signal intensity
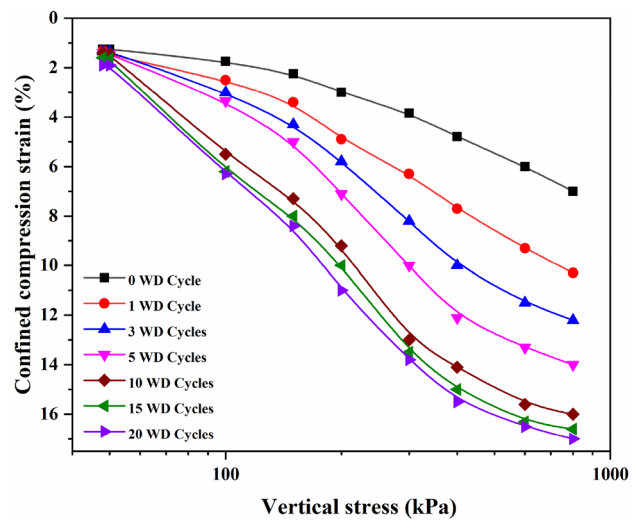

Fig. 11 Relationship between the confined compression strain and vertical stress

as the number of cycles increases: the largest difference between compression curves in terms of compression strain is between the sample subject to 1 WD cycle and the sample not subjected to any cycle; to obtain the same difference in terms of confined compression strain, it is necessary to pass from 3 to 10 WD cycles. After 10 WD cycles, the material seems not significantly affected anymore by previous wetting–drying cycles, consistently to the evidences about microstructure evolution.

In order to show the compression curve also in terms of void ratio, the void ratio at the beginning of the loading process has been estimated. The void ratio at the beginning of the mechanical loading has been obtained via the cumulative NMR intensity curves shown in the "Pore size distribution of loess samples after WD cycles" section, being the amplitude of the ^{1}H protons NMR signal in water molecules of the loess sample proportional to water content (Houston et al. 2001). In this study, the cumulative NMR intensity of the saturated compacted loess sample not subjected to any WD cycle is 62,752.51 ms, corresponding to a void ratio of 1.007: accordingly, the void ratios after 1, 3, 5, 10, 15, 20 are 1.041, 1.095, 1.118, 1.156, 1.159, and 1.162, respectively. Figure 12 shows the compression curves after different numbers of WD cycles in the void ratio vs vertical stress plane. It is interesting to note that all compression curves tend to the same logarithmic compliance for stress larger than 400 kPa, while for lower stresses the samples corresponding to more than 10 WD cycles exhibit a sort of volumetric collapse before stabilization. This is consistent with the reduction in cementation strength of the loess structure with WD cycles (see Fig. 4) and the increase in the pore volume between the particles (Fig. 9). Accordingly, a lower yield stress of the compacted loess with WD cycles is obtained, together with a larger compressibility in the immediate post-yield stage.
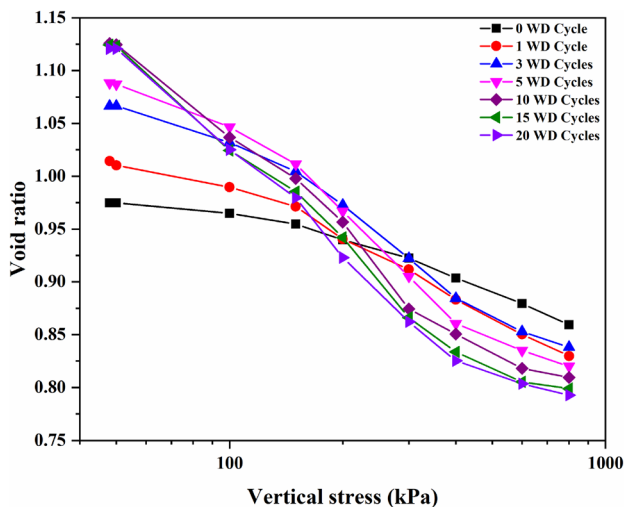

Fig. 12 Compression curves for different WD cycles

The effect of WD cycles on compression behavior of loess

Based on the above results, it can be concluded that the different compression behavior of compacted loess after WD cycles can be strongly linked to microstructure changes in the loess structure, which affect its macroscopic mechanical properties. With the increasing numbers of WD cycles, microstructure changes have been identified in the following three aspects: surface groups, contact relations, and pore size distribution. During the WD cycle, the soluble salts of loess structure will dissolve into water, which leads to an increase in the volume of the inter-aggregate pores. Meanwhile, part of the clay particles on the surface of the aggregates detaches from the aggregates toward the water, possibly leading to an increase in the volume of inter-aggregate pores and a decrease in the intra-aggregate pores. Furthermore, the amount of salts on the surface of loess particles was reduced, leading to the decreasing numbers of surface hydroxyl groups for loess particles. As a consequence, the hydrogen bond between the hydroxyl groups is weakened, reducing the interaction among loess particles. The WD cycles will also cause part of the clay particles to move, so that the connection between the compacted loess aggregates will be converted from "face to face" to "point to point." However, the particle size remained quite stable, and does not shows relevant changes as a consequence of WD cycles. The decrease of loess particle cementation strength, the change in the contacts between aggregates from "face to face" to "point to point," and the increase in macroporosity may be considered the main reasons for the changes in the compression behavior of compacted loess after WD cycles.

Conclusions

A series of experimental tests investigating the microstructural changes of compacted loess subjected to WD cycles were conducted, with the aim of identifying their role on the subsequent mechanical response. The increasing number of WD cycles weakens the interaction between adjacent loess particles, influencing the macroscopic response of loess specimens in terms of compression behavior. Despite WD cycles seem to not affect the particles size distribution of loess samples, WD cycles are capable of inducing measurable alterations of the surface hydroxyl groups, contact relations, and pore volume distribution.

During the WD cycle processes, the salts between adjacent loess particles transfer to the surface of loess, leading to a decrease of the number of surface hydroxyl groups between adjacent loess particles. The decreasing numbers in surface hydroxyl groups between adjacent loess particles reduce the interactions between adjacent particles, because

the hydrogen bonds between the hydroxyl groups are weakened. The interaction among adjacent loess aggregates has been found to pass from "face to face" to "point to point," forming inter-aggregate pores between aggregates. NMR results showed in fact that, as the number of WD cycles increases, the intra-aggregate pore volume decreases, while the inter-aggregate volume increases. A consistent microstructural picture has thus been provided, including cementation strength, aggregate contact relation, and pore size distribution, to justify the major role of WD cycles on the one-dimensional compression behavior of compacted loess.

Author contribution Wankui Ni and Xiangfei Lü designed research; Kangze Yuan performed all experiments and analyzed the data; Yongpeng Nie, Haiman Wang, Lan Li, and Kangze Yuan calculated the pore distribution of loess samples. Kangze Yuan and Xiangfei Lü wrote the paper. Gabriele Della Vecchia revised the manuscript. The map data in Fig. 1 was provided by the Data Center for Resources and Environmental Science, Chinese Academy of Science (RESDC) (http://www.resdc.cn). All authors read and approved the final manuscript.

Declarations

Ethics approval and consent to participate This article does not contain any studies with human participants and/or animals. Informed consent was obtained from all individual participants included in the study.

Conflict of interest The authors declare no conflict of interest.

References

Ahmed S, Lovell CW Jr, Diamond S (1974) Pore sizes and strength of compacted clay. J Geotech Eng Div 100(4):407–425

Arthur E, Schjønning P, Moldrup P et al (2013) Density and permeability of a loess soil: long-term organic matter effect and the response to compressive stress. Geoderma 193–194:236–245. https://doi.org/10.1016/j.geoderma.2012.09.001

ASTM (2006) Annual book of ASTM standards. ASTM International, West Conshohocken, PA

ASTM. D2974-07a (2007) Standard test methods for moisture, ash, and organic matter of peat and other organic soils; ASTM International: West Conshohocken, PA

Azizi A, Musso G, Jommi C (2020) Effects of repeated hydraulic loads on microstructure and hydraulic behaviour of a compacted clayey silt. Can Geotech J 57:100–114. https://doi.org/10.1139/cgj-2018-0505

Bai X (1992) Microstructural deformation of clay. University of Glasgow

Chen H, Wang J (2014) Regression analyses for the minimum intensity-duration conditions of continuous rainfall for mudflows triggering in Yan'an, northern Shaanxi (China). Bull Eng Geol Environ 73:917–928. https://doi.org/10.1007/s10064-013-0567-3

Costabel S, Yaramanci U (2013) Estimation of water retention parameters from nuclear magnetic resonance relaxation time distributions. Water Resour Res 49:2068–2079. https://doi.org/10.1002/wrcr.20207

Dathe A, Eins S, Niemeyer J, Gerold G (2001) The surface fractal dimension of the soil–pore interface as measured by image analysis. Geoderma 103:203–229. https://doi.org/10.1016/S0016-7061(01)00077-5

Delage P, Pellerin FM (1984) Influence de la lyophilisation sur la structure d'une argile sensible du Québec. Clay Miner 19(2):151–160

Della Vecchia G, Dieudonné AC, Jommi C, Charlier R (2015) Accounting for evolving pore size distribution in water retention models for compacted clays. Int J Numer Anal Meth Geomech 39(7):702–723

Fang XW, Shen CN (2013) Quantitative analysis of microstructure characteristics of Pucheng loess in Shaanxi province. Chin J Rock Mech Eng 32:1917–1925

Hong ZS, Yin J, Cui YJ (2010) Compression behaviour of reconstituted soils at high initial water contents. Géotechnique 60:691–700. https://doi.org/10.1680/geot.09.P.059

Houston SL, Houston WN, Zapata CE, Lawrence C (2001) Geotechnical engineering practice for collapsible soils. In: Toll DG (ed) Unsaturated Soil Concepts and Their Application in Geotechnical Practice. Springer, Netherlands, Dordrecht, pp 333–355

Hu Z, Cheng YZ (2017) Effectiveness of non-suction controlled method of wetting-drying cycles for unsaturated compacted loess material. KEM 748:346–349. https://doi.org/10.4028/www.scientific.net/KEM.748.346

Huang CQ, Wang MN, Tan WF et al (2018) Hydroxy-interlayered minerals in the Holocene paleosol on the southernmost Loess Plateau, China. Appl Clay Sci 153:70–77. https://doi.org/10.1016/j.clay.2017.12.007

Kleinberg RL (1996) Utility of NMR T2 distributions, connection with capillary pressure, clay effect, and determination of the surface relaxivity parameter ρ2. Magn Reson Imaging 14:761–767. https://doi.org/10.1016/S0730-725X(96)00161-0

Kleinberg RL, Flaum C, Griffin DD et al (2003) Deep sea NMR: Methane hydrate growth habit in porous media and its relationship to hydraulic permeability, deposit accumulation, and submarine slope stability: DEEP SEA NMR. J Geophys Res. https://doi.org/10.1029/2003JB002389

Kong L, Sayem HM, Tian H (2018) Influence of drying–wetting cycles on soil-water characteristic curve of undisturbed granite residual soils and microstructure mechanism by nuclear magnetic resonance (NMR) spin-spin relaxation time (T2) relaxometry. Can Geotech J 55:208–216. https://doi.org/10.1139/cgj-2016-0614

Li G, Wang F, Ma W, et al (2018) Variations in strength and deformation of compacted loess exposed to wetting-drying and freeze-thaw cycles. Cold Regions Science and Technology 151:159–167. https://doi.org/10.1016/j.coldregions.2018.03.021

Li P, Vanapalli S, Li T (2016) Review of collapse triggering mechanism of collapsible soils due to wetting. J Rock Mech Geotech Eng 8:256–274. https://doi.org/10.1016/j.jrmge.2015.12.002

Li XA, Li L, Song Y et al (2019) Characterization of the mechanisms underlying loess collapsibility for land-creation project in Shaanxi Province, China—a study from a micro perspective. Eng Geol 249:77–88. https://doi.org/10.1016/j.enggeo.2018.12.024

Liu YF (2016) Spatial and temporal variation of different precipitation type in the Loess Plateau area. Sci Geograph Sin 36(8):1227–1233

Lu H, Li J, Wang W, Wang C (2015) Cracking and water seepage of Xiashu loess used as landfill cover under wetting–drying cycles. Environ Earth Sci 74:7441–7450. https://doi.org/10.1007/s12665-015-4729-4

Lv Q, Wang S, Wang D, Wu Z (2014) Water stability mechanism of silicification grouted loess. Bull Eng Geol Environ 73:1025–1035. https://doi.org/10.1007/s10064-014-0646-0

Ma F, Yang J, Bai X (2017) Water sensitivity and microstructure of compacted loess. Transp Geotech 11:41–56. https://doi.org/10.1016/j.trgeo.2017.03.003

Ma T, Wei C, Yao C, Yi P (2020) Microstructural evolution of expansive clay during drying–wetting cycle. Acta Geotech 15:2355–2366. https://doi.org/10.1007/s11440-020-00938-4

Mao YC, Li GY, Lei JX et al (2013) Experimental study on the effects of wetting-drying cycles of compacted loess. AMR 831:326–330. https://doi.org/10.4028/www.scientific.net/AMR.831.326

Mariri M, Ziaie Moayed R, Kordnaeij A (2019) Stress–strain behavior of loess soil stabilized with cement, zeolite, and recycled polyester fiber. J Mater Civ Eng 31:04019291. https://doi.org/10.1061/(ASCE)MT.1943-5533.0002952

Meng J, Li X-A (2019) Effects of carbonate on the structure and properties of loess and the corresponding mechanism: an experimental study of the Malan loess, Xi'an area, China. Bull Eng Geol Environ 78:4965–4976. https://doi.org/10.1007/s10064-018-01457-z

Mu QY, Dong H, Liao HJ et al (2020) Water-retention curves of loess under wetting−drying cycles. Géotech Lett 10:135–140. https://doi.org/10.1680/jgele.19.00025

Musso G, Azizi A, Jommi C (2020) A microstructure-based elastoplastic model to describe the behaviour of a compacted clayey silt in isotropic and triaxial compression. Can Geotech J 57(7):1025–1043

National standards of People's Republic of China (1999) Standard for soil Test Methods (GB/TS0123-99). China Planning Press, Beijing

Ni W, Yuan K, Lü X, Yuan Z (2020) Comparison and quantitative analysis of microstructure parameters between original loess and remoulded loess under different wetting-drying cycles. Sci Rep 10:5547. https://doi.org/10.1038/s41598-020-62571-1

Nicolli HB, Bundschuh J, García JW et al (2010) Sources and controls for the mobility of arsenic in oxidizing groundwaters from loess-type sediments in arid/semi-arid dry climates—evidence from the Chaco-Pampean plain (Argentina). Water Res 44:5589–5604. https://doi.org/10.1016/j.watres.2010.09.029

Ono S, Sawano K, Kazama M (2020) Assessing the degree of slaking deterioration of rock materials by focusing on grain refinement. In: Duc Long P, Dung NT (eds) Geotechnics for Sustainable Infrastructure Development. Springer Singapore, Singapore, pp 1107–1112

Pinyol N, Vaunat J, Alonso EE (2007) A constitutive model for soft clayey rocks that includes weathering effects. Géotechnique 57:137–151. https://doi.org/10.1680/geot.2007.57.2.137

Qi J, Ma W, Song C (2008) Influence of freeze–thaw on engineering properties of a silty soil. Cold Reg Sci Technol 53:397–404. https://doi.org/10.1016/j.coldregions.2007.05.010

Romero E, Della Vecchia G, Jommi C (2011) An insight into the water retention properties of compacted clayey soils. Géotechnique 61:313–328. https://doi.org/10.1680/geot.2011.61.4.313

Romero E, Simms PH (2008) Microstructure investigation in unsaturated soils: a review with special attention to contribution of mercury intrusion porosimetry and environmental scanning electron microscopy. Geotech Geol Eng 26(6):705–727

Rosone M, Ferrari A, Celauro C (2018) On the hydro-mechanical behaviour of a lime-treated embankment during wetting and drying cycles. Geomech Energy Environ 14:48–60. https://doi.org/10.1016/j.gete.2017.11.001

Rost KT (2001) Late Holocene loess deposits and dust accumulation in the alpine meadow belt of the Wutai Shan, China. Quatern Int 76–77:85–92. https://doi.org/10.1016/S1040-6182(00)00092-6

Russ JC (1992) Characterizing and modelling fractal surfaces. J Comput Assisted Micro 4:73–126

Shao X, Zhang H, Tan Y (2018) Collapse behavior and microstructural alteration of remolded loess under graded wetting tests. Eng Geol 233:11–22. https://doi.org/10.1016/j.enggeo.2017.11.025

Shi H, Shao M (2000) Soil and water loss from the Loess Plateau in China. J Arid Environ 45:9–20. https://doi.org/10.1006/jare.1999.0618

Sun D, Bloemendal J, Rea DK et al (2004) Bimodal grain-size distribution of Chinese loess, and its palaeoclimatic implications. Catena 55:325–340. https://doi.org/10.1016/S0341-8162(03)00109-7

Sun H, Mašín D, Najser J et al (2020) Fractal characteristics of pore structure of compacted bentonite studied by ESEM and MIP methods. Acta Geotech 15:1655–1671. https://doi.org/10.1007/s11440-019-00857-z

Tian H, Wei C, Wei H et al (2014) An NMR-based analysis of soil–water characteristics. Appl Magn Reson 45:49–61. https://doi.org/10.1007/s00723-013-0496-0

Vandenberghe J (2013) Grain size of fine-grained windblown sediment: a powerful proxy for process identification. Earth Sci Rev 121:18–30. https://doi.org/10.1016/j.earscirev.2013.03.001

Vasava HB, Gupta A, Arora R, BhabaniS D (2019) Assessment of soil texture from spectral reflectance data of bulk soil samples and their dry-sieved aggregate size fractions. Geoderma 337:914–926. https://doi.org/10.1016/j.geoderma.2018.11.004

Wang F, Li G, Ma W et al (2020a) Effect of repeated wetting-drying-freezing-thawing cycles on the mechanic properties and pore characteristics of compacted loess. Adv Civ Eng 2020:1–8. https://doi.org/10.1155/2020/8839347

Wang G, Ye W, Lv Y (2019a) Loess geoheritage and geohazard protective measures at Luochuan Loess National Geopark in NW China. Geoheritage 11:1089–1100. https://doi.org/10.1007/s12371-019-00354-5

Wang HB, Zhou B, Wu SR et al (2011) Characteristic analysis of large-scale loess landslides: a case study in Baoji City of Loess Plateau of Northwest China. Nat Hazards Earth Syst Sci 11:1829–1837. https://doi.org/10.5194/nhess-11-1829-2011

Wang JD, Li P, Ma Y et al (2020b) Change in pore-size distribution of collapsible loess due to loading and inundating. Acta Geotech 15:1081–1094. https://doi.org/10.1007/s11440-019-00815-9

Wang JD, Li P, Ma Y, Vanapalli SK (2019b) Evolution of pore-size distribution of intact loess and remolded loess due to consolidation. J Soils Sediments 19:1226–1238. https://doi.org/10.1007/s11368-018-2136-7

Yao W, Li C, Zhan H et al (2020a) Multiscale study of physical and mechanical properties of sandstone in Three Gorges Reservoir region subjected to cyclic wetting–drying of Yangtze River water. Rock Mech Rock Eng 53:2215–2231. https://doi.org/10.1007/s00603-019-02037-7

Yao Z, Chen Z, Fang X et al (2020b) Elastoplastic damage seepage–consolidation coupled model of unsaturated undisturbed loess and its application. Acta Geotech 15:1637–1653. https://doi.org/10.1007/s11440-019-00873-z

Yu B, Liu G, Liu Q et al (2019) Seasonal variation of deep soil moisture under different land uses on the semi-arid Loess Plateau of China. J Soils Sediments 19:1179–1189. https://doi.org/10.1007/s11368-018-2119-8

Zhang D, Wang J, Chen C, Wang S (2020) The compression and collapse behaviour of intact loess in suction-monitored triaxial apparatus. Acta Geotech 15:529–548. https://doi.org/10.1007/s11440-019-00829-3

Zhang, W., Guo, A., Lin, C. (2019). Effects of cyclic freeze and thaw on engineering properties of compacted loess and lime-stabilized loess. Journal of materials in civil engineering, 31(9), 04019205. https://doi.org/10.1016/j.trgeo.2019.100279

Zhang X, Mavroulidou M, Gunn MJ (2017) A study of the water retention curve of lime-treated London Clay. Acta Geotech 12:23–45. https://doi.org/10.1007/s11440-015-0432-6

Zhu Y, Luo P, Zhang S, Sun B (2020) Spatiotemporal analysis of hydrological variations and their impacts on vegetation in semi-arid areas from multiple satellite data. Remote Sens 12:4177. https://doi.org/10.3390/rs12244177